

EVOLUTION OF THE SPIN OF LATE-TYPE GALAXIES CAUSED BY GALAXY-GALAXY INTERACTIONS

JEONG-SUN HWANG^{1,2}, CHANGBOM PARK³, SOO-HYEON NAM⁴, AND HAEUN CHUNG⁵

¹ Department of Physics and Astronomy, Sejong University, Seoul 05006, Korea; hwang2k@gmail.com
² Department of Science Education, Gwangju National University of Education, Gwangju 61204, Korea

³ School of Physics, Korea Institute for Advanced Study, Seoul 02455, Korea

⁴ Department of Physics, Korea University, Seoul 02841, Korea and

⁵ University of Arizona, Steward Observatory, 933 N Cherry Ave, Tucson, AZ 85721, USA

Draft version February 18, 2022

ABSTRACT

We use N-body/hydrodynamic simulations to study the evolution of the spin of a Milky Way-like galaxy through interactions. We perform a controlled experiment of co-planner galaxy-galaxy encounters and study the evolution of disk spins of interacting galaxies. Specifically, we consider the cases where the late-type target galaxy encounters an equally massive companion galaxy, which has either a late or an early-type morphology, with the closest approach distance of about 50 kpc, in prograde or retrograde sense. By examining the time change of the circular velocity of the disk material of the target galaxy from each case, we find that the target galaxy tends to lose the spin through prograde collisions but hardly through retrograde collisions, regardless of the companion galaxy type. The decrease of the spin results mainly from the deflection of the orbit of the disk material by tidal disruption. Although there is some disk material which gains the circular velocity through hydrodynamic as well as gravitational interactions or by transferring material from the companion galaxy, it turns out that the amount of the material is generally insufficient to increase the overall galactic spin under the conditions we set. It is found that the spin angular momentum of the target galaxy disk decreases by 15 - 20% after a prograde collision. We conclude that the accumulated effects of galaxy-galaxy interactions will play an important role in determining the total angular momentum of late-type galaxies at current stage.

Subject headings: galaxies: spiral — galaxies: kinematics and dynamics — galaxies: evolution — galaxies: interactions — methods: numerical

1. INTRODUCTION

The spin of galaxies is an important quantity to understand the evolution of galaxies over cosmic time. Starting from the tidal torque theory (Hoyle 1949; Peebles 1969; White 1984), it has been proposed that galaxies acquire angular momentum via the tidal field from surrounding galaxies. In the Lambda Cold Dark Matter (ΛCDM) paradigm, galaxies are first formed in dark matter (DM) halo and evolved through continuous merging and interacting with nearby galaxies while gaining or losing mass and angular momentum. In particular, it is vital to understand how the angular momentum of late-type galaxies (LTGs) are being evolved over cosmic time, because the LTGs are considered as building blocks under the hierarchical merging scenario. For example, the existence of a relatively new population of rotation-supported early-type galaxies (ETGs) can not be fully explained without understanding the role of LTG spin evolution (Emsellem et al. 2011; Cappellari 2016; Graham et al. 2018).

Previous studies have shown that the spin of galaxies is also correlated with environments such as distance to the neighbour, axes of large-scale structure, 2D correlation, and clustering (Porciani et al. 2002; Davis & Narayanan 2009; Tempel et al. 2013; Casuso & Beckman 2015; Codis et al. 2015; Lee et al. 2018b). More recent studies have demonstrated how the angular momentum acquired through merging can affect the galaxy evolution (Brook et al. 2012; Cloet-Osselaer et al. 2014; Rodriguez-Gomez

et al. 2017).

There has also been some effort to measure any correlations between the spins in pairs of spiral galaxies. For example, Cervantes-Sodi et al. (2010) have estimated the spin parameter for 3624 LTGs (target galaxies) at low redshift, identified using the Sloan Digital Sky Survey (SDSS). They have discovered a statistically significant correlation between the spin magnitudes of neighbouring galaxies. Specifically, they have found that the values of the spin parameter of the late-type target galaxies decrease as a companion galaxy (the nearest neighbour of a comparable size) approaches, regardless of the companion morphology, although the decrease of the spin parameter appeared more clearly when the companion is a late-type rather than an early-type (refer to their Figures 3 and 4). Particularly noteworthy is that the decrease of the spin parameter begins to operate as soon as the (projected) separation between the pair becomes smaller than the virial radius of the companion, implying interactions could have caused the decrease.

More recently, using the data of Mapping Nearby Galaxies at APO (MaNGA), Lee et al. (2018a) have estimated the spin parameter for 1830 low-redshift galaxies from the analysis of two-dimensional stellar spectra. They divided the galaxies into four groups by the morphological type of the target as well as the companion (the nearest influential neighbour). As shown in their Figure 7, in the case of late-type targets having an early-type companion (“L-e”), the spin parameter of the target galaxies has been found to be decreased clearly when

the pair separation becomes less than the virial radius of the companion. (In the case of late-type targets having a late-type companion, “L-I”, such decrease has not been found clearly in the spin of the targets. However, it should be noted that the number of close pairs in this case is smaller than that in L-e case.)

The aforementioned observational studies that have shown some interesting correlations between the spins in pair of galaxies (Cervantes-Sodi et al. 2010; Lee et al. 2018a) motivated us to explore the evolution of the spin of galaxies by using numerical simulations. With the aim of finding physical mechanism for changing the angular momentum of galaxies, we have been performing a series of N -body/hydrodynamic simulations of interactions between galaxies in a variety of environments. (We generally refer to “angular momentum” as “spin angular momentum”, if not specified.)

In this paper, we present the results of our first set of simulations concerning the evolution of the spin of a Milky Way-like LTG (target galaxy) that experiences an interaction with a neighbour (companion galaxy). Specifically, we have conducted simulations of co-planner galaxy-galaxy interactions, where the target galaxy encounters an equally massive companion galaxy, which has either a late- or an early-type morphology, in prograde or retrograde sense. We also have performed a simulations of the target galaxy evolving in isolation for comparison. The simple configuration for this work is intended to focus on examining the effects that the different companion morphology (late-type vs. early-type) and the encounter geometry (prograde vs. retrograde) might have on the spin evolution of the target galaxy, in comparison with that of the isolated target galaxy. As motivated by observations, this work aims at examining what happened on the spin of the target galaxy. We expect the results of this first set of simulations to serve as a basis for our more extended follow-up studies and also for other related works.

The outline of this paper is as follows. We begin in Section 2 with an overview of the galaxy models and the simulation code used for this work. We then describe the initial conditions of our simulations. In Section 3, we present the results of our simulations focusing on the structural and the kinematic evolution of the target galaxy from each of our runs. Finally in Section 4, we summarise and discuss our findings. We also highlight the limitations and the implications of our results.

2. MODEL DESCRIPTION

2.1. Galaxy Models

For this numerical study, we use two galaxy models - a LTG model “L” and an ETG model “EH”. Model L is the same model used in our previous work (Hwang et al. 2018; hereafter Paper I). Model EH is similar to model EH in paper I but has half the mass of the previous model. Thus models L and EH in this work have the same mass. Both models L and EH are generated by using the ZENO¹ software package (Barnes 2011; see also Hwang et al. 2013 for the generation procedure). As the detailed description of the models is presented in Paper I (see also Hwang et al. 2013), here we briefly outline their

key properties.

Model L resembles the Milky Way Galaxy in size and mass, with the total mass of $M_{\text{tot}} = 1.27 \times 10^{12} M_{\odot}$ and the virial radius of $R_{\text{vir}} = 214$ kpc (Table 1). The model consists of four components - a stellar disk, a gas disk, a stellar bulge, and a DM halo. The star and gas disks have the masses of $M_{\text{ds}} = 5.2 \times 10^{10} M_{\odot}$ and $M_{\text{dg}} = 0.8 \times 10^{10} M_{\odot}$, respectively (McMillan 2011; Kubryk et al. 2015). The disk gas fraction in mass, $f_{\text{dg}} = M_{\text{dg}}/(M_{\text{ds}} + M_{\text{dg}})$, is thus about 0.13. Both disks follow an exponential surface density profile and a sech² vertical profile (Equation (1) in paper I). The radial scale lengths of the stellar and gaseous disks are $r_{\text{ds}} = 3.5$ kpc and $r_{\text{dg}} = 8.75$ kpc, respectively, and the vertical scale length of both disks is $z_{\text{ds}} = z_{\text{dg}} = 0.35$ kpc (refer to Hwang et al. 2013 for the justifications of the parameter values). The number of particles distributed on the star and gas disks are $N_{\text{ds}} = 122\,880$ and $N_{\text{dg}} = 32\,768$, respectively. Both disks are initialized with an either clockwise or counter-clockwise directional spin, as necessary. The disk gas particles are set to rotate with the local circular velocities. On the other hand, the disk star particles are given to have the radial and vertical dispersions in addition to the local circular velocities as described in Barnes & Hibbard (2009). In Figure 1, we show the initial distribution of the disk star and gas particles of model L and the circular and radial velocity (v_c and v_R , respectively) profiles of the disk star and gas particles. (Hereafter, we refer to the azimuthal and the radial velocities in the cylindrical coordinate system as the circular and the radial velocities (v_c and v_R), respectively. The positive directions of v_c and v_R are set to the direction of the initial disk rotation and the radially outward direction, respectively.) The temperature of the disk gas particles are set uniformly to $T = 10\,000$ K. The bulge component has the total mass of $M_b = 1.0 \times 10^{10} M_{\odot}$. It follows the Hernquist profile (Hernquist 1990) with truncation at large radii as presented in Paper I (Equation (2)). The number of particles of the bulge component is $N_b = 24\,567$. The DM halo component follows a Navarro et al. (1996) model with an exponential taper at large radii (Equation (3) in Paper I). The total mass of the DM halo is $M_{\text{hd}} = 120 \times 10^{10} M_{\odot}$ and the number of particles is $N_{\text{hd}} = 655\,360$. The DM halo and the bulge components are dispersion-supported with no appreciable rotation (Barnes & Hibbard 2009; von Neumann 1951).

The ETG model EH has the total mass of $M_{\text{tot}} = 1.27 \times 10^{12} M_{\odot}$ (which is equal to that of model L, as intended) and the virial radius of $R_{\text{vir}} = 250$ kpc. The model possesses three components, a stellar bulge, a DM halo, and a gaseous halo, with the masses of $M_b = 7.0 \times 10^{10} M_{\odot}$, $M_{\text{hd}} = 118.8 \times 10^{10} M_{\odot}$, and $M_{\text{hg}} = 1.2 \times 10^{10} M_{\odot}$ (Anderson & Bregman 2010), respectively. The gas fraction in the halo is $f_{\text{hg}} = M_{\text{hg}}/(M_{\text{hd}} + M_{\text{hg}}) = 0.01$. The bulge and the DM halo components follow the Hernquist model (Hernquist 1990) and a Navarro et al. (1996) model, respectively, and are dispersion-supported as in model L. The gas halo follows a nonsingular isothermal profile with a taper (Equation (3) in paper I). The temperature of the halo gas particles are determined by the hydrostatic equilibrium (refer to Figure 2 of Paper I). The initial velocity of the halo gas is set to zero. The number of particles distributed in each component is $N_b = 172\,032$, $N_{\text{hd}} =$

¹ <http://www.ifa.hawaii.edu/~barnes/software.html>

TABLE 1
 MODEL PARAMETERS

Model	M_{tot}^a	R_{vir}^b	M_{ds}	M_{dg}	M_{b}	M_{hd}	M_{hg}	f_{dg}	f_{hg}	N_{ds}	N_{dg}	N_{b}	N_{hd}	N_{hg}
L	127.0	214.0	5.2	0.8	1	120.0	...	0.13	...	122 880	32 768	24 567	655 360	...
EH	127.0	250.0	7.0	118.8	1.2	...	0.01	172 032	655 360	49 152

Masses are in units of $10^{10} M_{\odot}$ and the virial radius is in units of kpc.

^a M_{tot} is the sum of the masses of all particles.

^b We use the virial radius R_{vir} as R_{200} , which is defined as the radius within which the average density is 200 times the critical density.

655 360, and $N_{\text{hg}} = 49 152$, respectively.

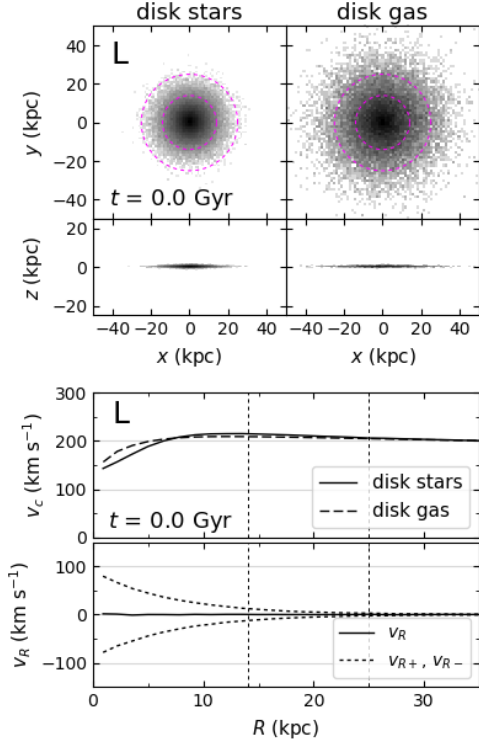


FIG. 1.— Top two rows: initial distribution of the disk particles of model L. The disk star and gas particles are displayed separately in the left and right columns, respectively. The upper and lower rows show the distribution projected on to the x-y and x-z plane, respectively. The gray scale represents the column densities of the star and gas disks. (The gray scale varies). The inner and outer dotted circles (magenta) drawn in the upper panels indicate R_{14} and R_{25} , respectively. Bottom two rows: initial profiles of the circular and the radial velocities (v_c and v_R , respectively) of the disk particles of model L. In the upper panel, the solid and dashed curves represent the mass weighted, cylindrically averaged azimuthal velocities of the disk stars and gas particles, respectively, with respect to the cylindrical radius R . In the lower panel, the solid curve shows the mass weighted, cylindrically averaged radial velocities of the stellar particles; the upper and lower dotted curves represent the average values of v_{R+} and v_{R-} of the star particles, respectively. For the gas, the radial velocity profile is not shown as it is zero at the initial time. In each panel, the two vertical dotted lines (black) indicate R_{14} and R_{25} . (The vertical velocity profile of the disk material is not shown, as it is not significant in our work.)

2.2. Simulation Code

To perform the numerical simulations, we make use of an early version of GADGET-3 N -body/smoothed particle hydrodynamics (SPH) code (originally described in Springel 2005). Here we briefly describe the simulation

code and refer interested readers to Springel & Hernquist (2003) and our previous papers for more details (paper I; Hwang & Park 2015).

The code computes the gravitational force using a tree algorithm (Barnes & Hut 1986) and the hydrodynamic force adopting a SPH method in the entropy conservative formulation (Springel & Hernquist 2002; Gingold & Monaghan 1977). The radiative cooling and heating are modeled considering the primordial mixture of hydrogen and helium by photoionization (Katz et al. 1996). Star formation and the associated supernova feedback in the interstellar medium (ISM) are implemented adopting the sub-resolution multiphase model of Springel & Hernquist (2003). A thermal instability operates for gas exceeding a threshold density and the ISM is treated as a statistical mixture of cold clouds and ambient hot medium. Stars form in dense regions consuming the cold clouds, and the consumption timescale is chosen to match the observations (Kennicutt 1998). Among the newly formed stars, massive stars (with the mass greater than $8 M_{\odot}$) die instantly as supernovae and release energy as heat to the ambient diffuse gas. Some cold clouds are also evaporated inside the supernova bubbles returning material to the ambient medium.

We set the code parameters governing star formation and feedback to the standard values of the multiphase model (Springel & Hernquist 2003). Some of the key values are as follows. The star formation time-scale and the mass fraction of massive stars among the newly formed stars are $t_0^* = 2.14$ Gyr and $\beta = 0.1$, respectively. The “supernova temperature” is $T_{\text{SN}} = 10^8$ and the temperature of cold clouds are $T_c = 1000$ K. The parameter value for supernova evaporation is $A_0 = 1000$.

The gravitational softening lengths for the particles of the star and gas disks, bulge, and DM and gas halos are set to 0.14, 0.11, 0.14, 0.30, and 0.11 kpc, respectively. These gravitational softening lengths are determined by considering the equivalence of the maximum acceleration experienced by a single particle in each component.

2.3. Initial conditions for our simulations

In order to study the spin evolution of a Milky Way-like LTG in different situations, we perform five numerical simulations (Table 2)²: Run L is the simplest one where the LTG model L (target galaxy) evolves in isolation. In runs LLp and LLr, model L (target) encounters another model L (companion) in prograde and retrograde

² Additionally, we have performed “run LLr2”. In this run, the late-type target galaxy encounters the late-type companion galaxy in retrograde sense, while both galaxies spin in counterclockwise direction. We present the results of this run in Appendix A.

TABLE 2
SIMULATIONS

Run	Target (spin ^a)	Companion (spin)	Interaction ^b
L	L (CW)
LLp	L (CW)	L (CW)	prograde
LLr	L (CCW)	L (CW)	retrograde
LEHp	L (CW)	EH	prograde
LEHr	L (CCW)	EH	retrograde

^a The direction of the spin of the disk of a LTG, when viewed from the positive z -axis. “CW” and “CCW” stand for clockwise and counterclockwise, respectively.

^b Whether a target galaxy experiences a collision with a companion galaxy as prograde or retrograde (see text for the details).

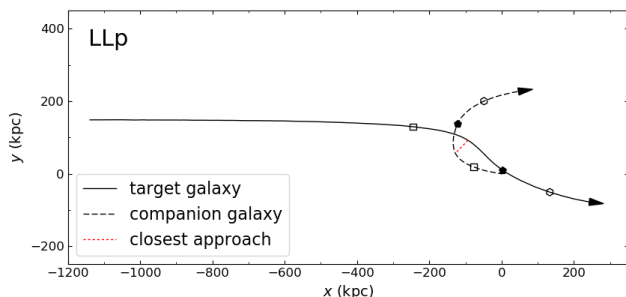


FIG. 2.— Orbital trajectories of the target (black solid line) and companion (black dashed line) galaxies in run LLp during 7 Gyr. (The orbital trajectories from the other runs LLr, LEHp, and LEHr are only slightly different from those shown here.) The target galaxy starts from $(x_0, y_0, z_0) = (-1140 \text{ kpc}, 150 \text{ kpc}, 0)$ with the initial velocity of $(v_{x0}, v_{y0}, v_{z0}) = (200 \text{ km s}^{-1}, 0, 0)$ and the companion galaxy from the origin with zero initial velocity. The target and companion galaxies meet most closely at $t = 4.5$ Gyr with the distance of about 50 kpc (red dotted line). The positions of the two galaxies at $t = 4, 5$, and 6 Gyr are marked on their orbits with open squares, filled pentagons, and open hexagons, respectively.

sense, respectively. Similarly, in runs LEHp and LEHr, model L (target) encounters the ETG model EH (companion) in prograde and retrograde sense, respectively. We construct the initial conditions of our simulations as below.

First, for the isolated case of run L, model L is initialized in the x - y plane (i.e., the midplane of the disk lies on the x - y plane), being placed the center of the model at the origin as shown in Figure 1 (top two rows). (We generally refer to “disk” as the total disk consisting of both stars and gas, if not specified such as “star disk” or “gas disk”.) The disk of model L in this run is set with a clockwise directional spin as viewed from the positive z -axis, and with zero (systemic) velocity.

Next, for runs LLp and LLr, the two LTG-LTG encounter simulations, model L as the target galaxy is initially placed at $(x_0, y_0, z_0) = (-1140 \text{ kpc}, 150 \text{ kpc}, 0)$ and another model L as the companion galaxy is positioned at the origin as presented in Figure 2. The initial velocity (v_{x0}, v_{y0}, v_{z0}) of the target and the companion galaxies are set to $(200 \text{ km s}^{-1}, 0, 0)$ and $(0, 0, 0)$, respectively. These initial positions and velocities of the models are chosen so that the two galaxies encounter most closely at $t = 4.5$ Gyr since the start of each run with the distance of about 50 kpc. The closest approach distance of

50 kpc is chosen to see some encounters that are not too weak or not too strong. For galaxies at low redshift and not in high-density regions like galaxy clusters, which are relevant to this study, distant encounters occur more frequently than very close encounters do. Although distant encounters are frequent, the effects of a single distant encounter on the evolution of a target galaxy would be weak. On the other hand, the effects of a single very close encounter would be significant, but such an encounter is rare. (Once it happens, the galaxies involved would merge quickly.) Thus, considering both frequency and effects of galaxy-galaxy interactions, choosing encounters at an “intermediate” strength would be reasonable for our work. In the initial conditions of runs LLp and LLr, the midplanes of the disks of both target and companion galaxies are located on the x - y plane. The only difference between the two initial conditions is the direction of the spin of the target galaxy: For run LLp, the disk of the target galaxy is set with a clockwise directional spin; whereas, for run LLr, it is set with a counterclockwise directional spin. In both runs, the disk of the companion galaxy is set with a clockwise directional spin.

Finally, for runs LEHp and LEHr, the two LTG-ETG encounter runs, the initial positions and velocities of the target and the companion galaxies are set with the same values as in runs LLp and LLr. The direction of the spin of the target galaxy in run LEHp(LEHr) is also set to clockwise(counterclockwise), as in run LLp(LLr). The only difference between the initial conditions of run LEHp(LEHr) and run LLp(LLr) is the morphological type of the companion galaxy, which is an early-type in runs LEHp and LEHr but a late-type in runs LLp and LLr.

3. SIMULATION RESULTS

With the initial conditions described in Section 2.3, we have performed five numerical simulations for $t = 7$ Gyr since the start of each run (Table 2). Here we present the results of our simulations. In the first subsection, we describe the general evolution of each run, focusing on the change in structure and star formation activity in the target galaxy. Then we examine the kinematics and the spin angular momentum of the target galaxy in the following subsections.

3.1. General Evolution

3.1.1. Run L

Figure 3 presents the distribution of the disk particles of the target galaxy from run L at four epochs. The target galaxy in this run evolves in isolation. As seen in the top row, a central bar and multiple spiral patterns develop in the star and gas disks as time passes. In the bottom two rows, star-forming gas particles are distinguished from non-star-forming gas particles by cyan and blue points, respectively. Most of star-forming gas appears in the relatively inner region of the disk, within the galactocentric (cylindrical) radius of $R = 14 \text{ kpc}$ (R_{14}), marked with a magenta dotted circle (the inner one). R_{14} is the radius within which $\sim 90\%$ of the disk stars were initially distributed in the model; it is also four times the initial radial scale length of the stellar disk. We will use R_{14} as a reference radius throughout this paper, for the purpose of indicating the region where most initial disk

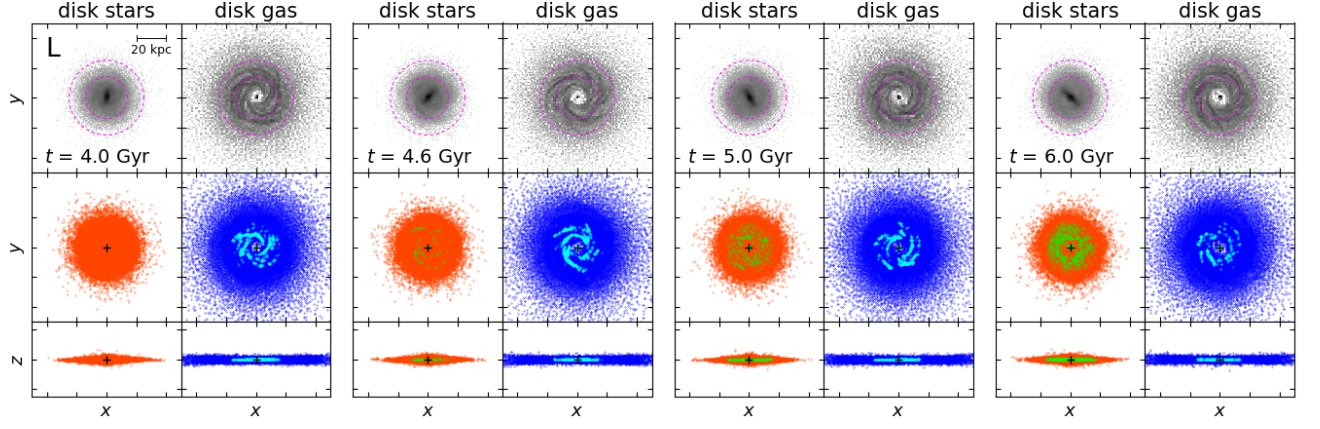


FIG. 3.— Four snapshots from run L of the disk particles of the target galaxy at $t = 4, 4.6, 5,$ and 6 Gyr (from leftmost two columns to rightmost two columns in order, respectively; refer to Figure 1 for the initial particle distribution). The star and gas particles at each epoch are displayed separately (left and right columns, respectively). The top row shows the column densities of the disks projected on to the x - y plane, with adaptive gray scales. The inner and outer dotted (magenta) circles drawn in each panel of the top row indicate R_{14} and R_{25} , respectively. The middle and bottom rows display the individual disk particles seen in the x - y and x - z planes, respectively, indicating the “status” of the particles with different colors: Orange points represent “old” disk stars (the stars originally set as the disk stars and the stars formed out of the disk gas before $t = 4.5$ Gyr) and green points denote “young” disk stars (the stars formed out of the disk gas at $t \geq 4.5$ Gyr). Blue and cyan points represent the non-star-forming (gas with zero star formation rate at the instant) and star-forming disk gas particles (gas having positive values of star formation rate at the instant), respectively. In each panel of the middle and bottom rows, the center of the target galaxy is marked with a plus sign.

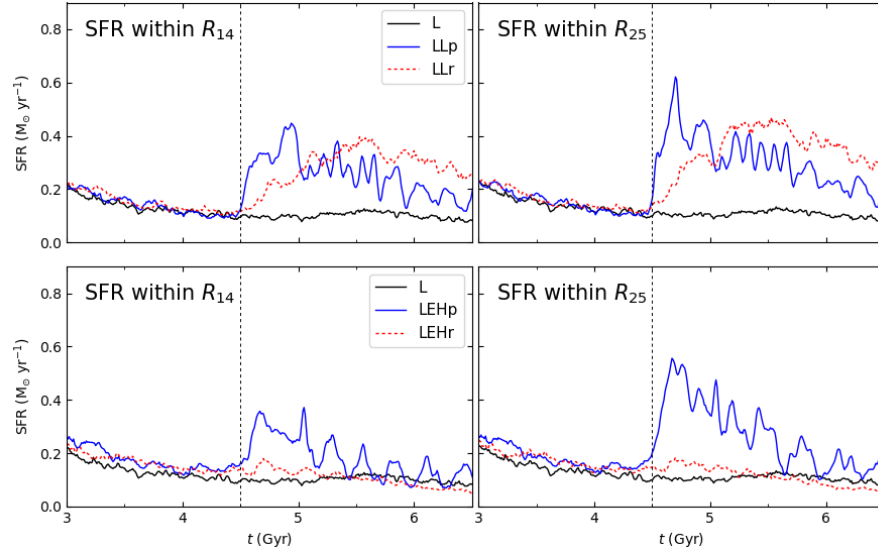


FIG. 4.— Evolution of the star formation rate (SFR) of the target galaxy from runs L, LLp, and LLr (top row) and from runs L, LEHp, and LEHr (bottom row). The left column shows the sum of the SFRs of the star-forming gas particles enclosed in a cylindrical regions of radius R_{14} (with $|z| \leq 20$ kpc), including the captured particles from the companion if there are any, while the right column displays those enclosed in a cylindrical region of radius R_{25} (with $|z| \leq 20$ kpc) from each run. The vertical dotted line in each panel indicates the closest approach time ($t = 4.5$ Gyr) between the target and the companion galaxies in the galaxy-galaxy encounter runs.

stars were located. We will also use another reference radius $R = 25$ kpc (R_{25} ; the outer dotted circle in the figure); it is half of the closest approach distance in the galaxy-galaxy encounter runs.

As star-forming gas subsequently turns into stars, the gaseous disk dissipates and the stellar disk grows in mass. Among those stars formed out of the star-forming gas, the stars formed after $t = 4.5$ Gyr are displayed with green points (hereafter, “young” (disk) stars), whereas those stars added onto the disk before $t = 4.5$ Gyr as well as the stars initially set as the disk stars are plotted with orange points (hereafter, “old” (disk) stars). The reason we divide the young and old stars based on whether they were formed after $t = 4.5$ Gyr or not is to

compare the distribution of the young stars in the isolated target galaxy with those in the target galaxies from the galaxy-galaxy encounter runs in the following subsections. We present in Figure 4 the sum of the SFRs of the individual star-forming gas particles within R_{14} and R_{25} . The SFR within R_{25} (and also that within R_{14}) does not greatly change, but generally decreases slowly as time passes, due to the accumulated effects of the cold gas consumption by star formation.

3.1.2. Run LLp

Figure 5 (top row) shows the large-scale configuration of the disks of both target and companion galaxies from run LLp, with their orbital trajectories overlaid. The

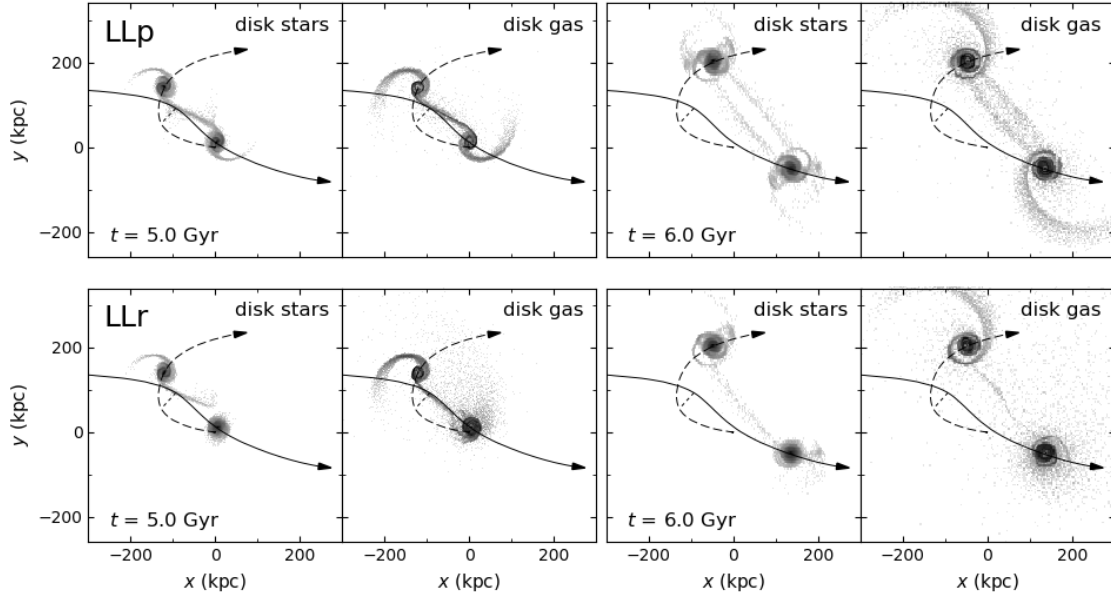


FIG. 5.— Large-scale snapshots from runs LLp (top row) and LLr (bottom row) at $t = 5$ (left two columns) and 6 Gyr (right two columns). In the snapshots from each run at each epoch, disk star and gas particles from both target and companion galaxies are presented separately (left and right panels, respectively). In each panel, the orbital trajectories of the target and companion galaxies, and the closest approach distance between the two galaxies are over-plotted (refer to Figure 2).

closest approach between the two LTGs occurs at $t = 4.5$ Gyr with the distance of about 50 kpc. When the target galaxy collides with the companion galaxy, it experiences the encounter as prograde, since the orbit of the companion is prograde with respect to the clockwise directional spin of the target. (By the same token, the companion galaxy, which is spinning in clockwise direction, also experiences the encounter with the target as prograde.) Thus, as seen in the large-scale snapshots taken after the collision, substantial bridges and counter-tails are pulled out of the stellar and gas disks of the target(companion) galaxy due to the tidal force imposed by the companion(target) galaxy. There is some mass exchange between the galaxies: Some disk star and gas particles, among those initially set as the disk particles of the companion, transfer to the target through the stellar and gas bridges formed out of the companion, and vice versa.

Focusing on the evolution of the target galaxy, Figure 6(a) provides more close-up views of the star and gas disks. The snapshots at $t = 4$ Gyr (i.e., 0.5 Gyr before the collision) appear to be similar to those from run L (without a collision) at the same epoch. However, the snapshots taken after the collision show big differences compared with those from run L at the corresponding epochs: At the onset of the collision, the star and gas disks of the target galaxy start to be pulled radially outward due to the tidal force. Here the tidal force not only stretches the target along the line connecting the target and the companion, but also compresses the target along the perpendicular direction. Besides, since gas interacts not only gravitationally but also hydrodynamically, the leading side of the gas disk of the target galaxy is shock-compressed by the collision with the gas disk of the companion galaxy. As seen in the snapshots at $t = 4.6$ Gyr (shortly after the collision), a lot of star-forming gas turns up along the interaction-induced arms through

the prograde collision. By $t = 5$ Gyr, substantial bridges and tails have developed out of both stellar and gas disks of the target galaxy. The higher gas density at the leading side of the gas disk and of the gas bridge results from the shock generated through the collision. Until $t = 6$ Gyr since the time of the collision, a lot more young stars have been added onto the disk, than in the isolated target galaxy from run L. As shown in Figure 4, the SFR in the target galaxy increases abruptly right after the collision, indicating that the strong star formation activity is triggered by the prograde collision. The SFR within R_{25} (considering the wider region) reaches the maximum after a few hundreds of mega years since the collision, and then starts to drop (but still much higher than that in run L until $t = 6$ Gyr) as gas is consumed by the burst of star formation.

3.1.3. Run LLr

The results from run LLr are presented in Figures 5 (bottom row) and 6(b). When the collision occurs at $t = 4.5$ Gyr, the target galaxy spinning counterclockwise direction experiences the collision as retrograde. (On the other hand, the companion galaxy spinning clockwise direction experiences it as prograde.) Due to the retrograde passage of the companion in this run (with respect to the spin of the target), tidal perturbations on the target by the companion act for a shorter time than in the case of the prograde collision (run LLp). Accordingly, the target galaxy here does not develop strong bridges and tails as seen in the large-scale snapshots. During the collision, some disk material which initially belonged to the companion is captured by the target galaxy.

Looking at the target galaxy more closely (Figure 6(b)), the amount of star-forming gas increases shortly after the collision (at $t = 4.6$ Gyr), more than in the isolated target galaxy from run L, but not as greatly as in the target galaxy from run LLp. It can also be

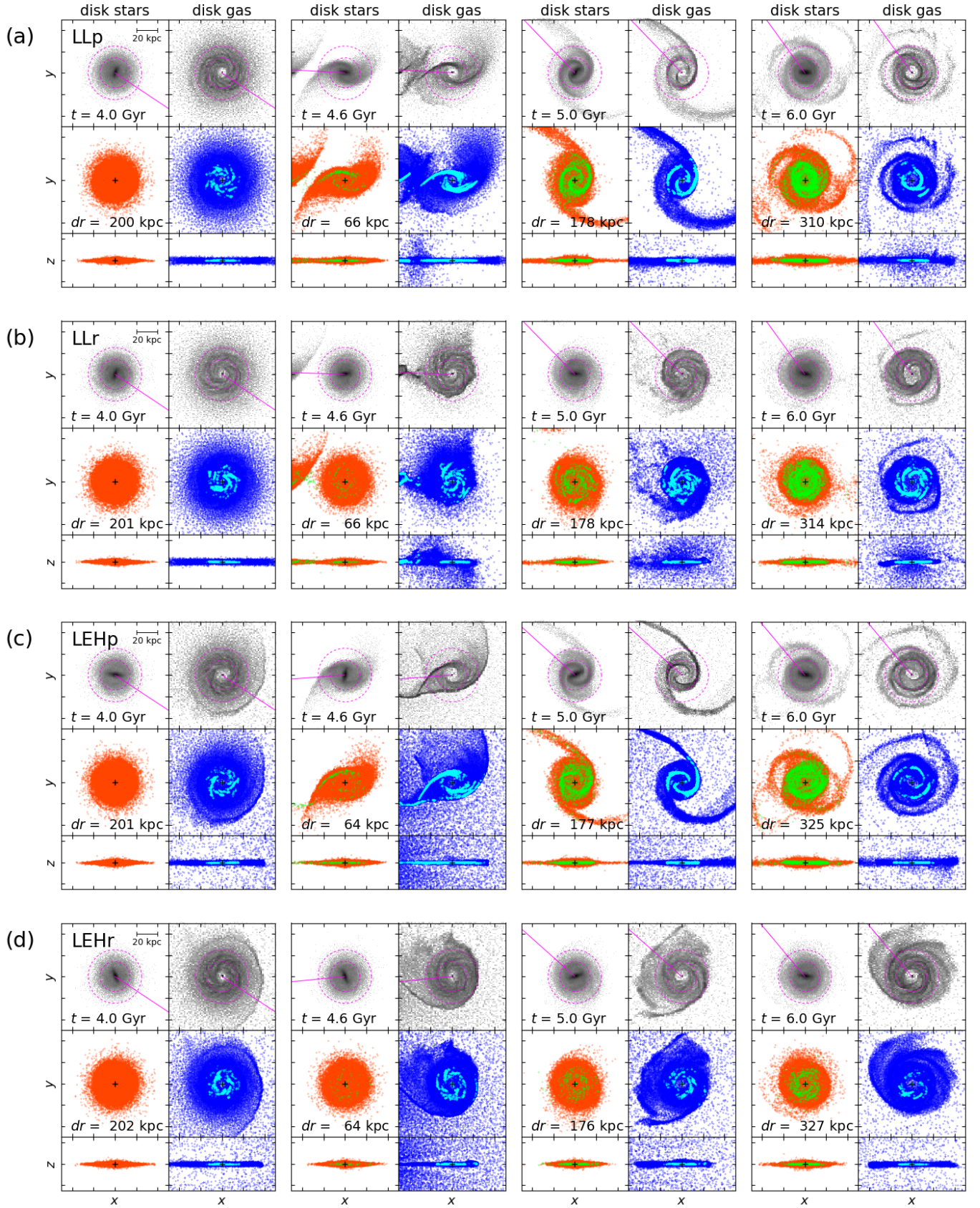


FIG. 6. — Same as Figure 3, but for runs LLp (a), LLr (b), LEHp (c), and LEHr (d). The snapshots presented here include any disk particles captured by the target galaxy from the companion galaxy, if there are any. In each panel of the top row of (a)-(d), the solid (magenta) line is drawn from the center of the target to the center of the companion. The distance between the two galaxies (dr) at each epoch is shown in the middle row of (a)-(d).

checked from the SFR presented in Figure 4. The SFR (within R_{25}) of the target galaxy in this run LLr increases after the collision, but less drastically than that in run LLp. Because of the less drastic increase of the star formation activity, cold gas in the target galaxy is consumed less quickly than in run LLp. This helps the target galaxy to maintain relatively active star formation until later times; the gas particles captured by the target galaxy during the collision also contribute to it. (The amount of gas captured by the target galaxy in run LLr is greater than that in run LLp, because in this particular case of run LLp the shock boundary generated between the two gas disks by the prograde collision hinders the flow of gas for a while. In general, the amount and the orbit of the material captured by one galaxy from the other are very sensitive to various factors such as the relative orbit of the pair, the physical properties of each galaxy, and so on. A detailed discussion on this subject is beyond the scope of this paper.)

3.1.4. Runs LEHp and LEHr

The snapshots from runs LEHp and LEHr are presented in Figure 6(c) and (d), respectively. In run LEHp(LEHr), the target galaxy spinning in clockwise(counterclockwise) direction experiences the collision with the early-type companion as prograde(retrograde). As seen in the snapshots, the distribution of the old disk stars (which are mainly affected by the gravitational force) in the target galaxy from run LEHp(LEHr) at each epoch is generally similar to that from run LLp(LLr) at the corresponding epoch, as expected. However, the distributions of the disk gas (which is influenced by both gravitational and hydrodynamic forces) and of the young stars (which are formed after the collision) are somewhat different from those from run LLp(LLr). The different hydrodynamic interactions between the disk gas of the target and either the halo gas of the companion (in runs LEHp and LEHr) or the disk gas of the companion (in runs LLp and LLr) may have caused the different distributions.

In run LEHp (Figure 6(c)), at $t = 4$ Gyr (0.5 Gyr before the closest approach), the gas disk of the target galaxy already starts to form a bow-like front as it comes under the influence of the extended gas halo of the companion galaxy. At $t = 4.6$ Gyr, shortly after the closest approach, the gas at the leading side of the disk is shock-compressed by the collision (c.f. run EH-L in Hwang & Park 2015). In addition, some disk gas is stripped by ram pressure (as seen at the rear side of the disk) or ionized and then scattered, as it moves against the diffuse hot halo gas of the companion. As displayed in Figure 4, the SFR (within R_{25}) of the target galaxy in run LEHp increases greatly by the prograde collision and then slows down afterwards due the cold gas consumption.

In the case of the retrograde collision (Figure 6(d)), the target galaxy in run LEHr does not develop bridges and tails out of the star and gas disks after the collision. The SFR of the target galaxy (Figure 4) increases during the collision but only slightly, compared with that of the target galaxy without a collision (run L). At later times ($t \gtrsim 5.5$ Gyr), the SFR in this run becomes even lower than that of the isolated target galaxy. It is because some cold gas is removed not only by star formation but also

by ram pressure and/or ionization in run LEHr.

3.2. Kinematics

Here we discuss the kinematics of the disk star and gas particles of the target galaxy from our five runs. First we examine the time change of the circular and radial velocities of the disk particles in the following four subsections. Then we look into the evolution of the spin angular momentum of the disk material in the last subsection.

3.2.1. Run L

Figures 7(a) and 8 (top row) present the profiles of the circular and radial velocities (v_c and v_R , respectively) of the disk particles of the target galaxy while evolving in isolation. As seen in the figures, the profiles of the stars and gas deviate somewhat from the initial ones via secular evolution (see Figure 1 for the initial profiles) - i.e., as a bar and spiral arms develop on the disk and star formation with the associated feedback comes into play. Although some changes appear in the velocity profiles as time passes, more for gas than for stars, in the relatively inner region of the disk (where star and structure formation occur more actively), the deviations are generally not significant throughout the run. (In general, the circular velocity profile of young disk stars could be different from that of (old) disk stars. For example, when they have just been formed, the profile may follow that of gas rather than that of stars. We do not display the profile of young stars separately in the figure, because their contribution to the overall (mass weighted) stellar velocity profile is not significant in our runs. It should also be noted that their contribution in luminosity could be more significant than in mass.)

In Figure 9, we compare the circular velocity profile of the disk stars and that of the entire disk material (stars + gas) at $t = 5$ and 6 Gyr (black solid curves). They appear to be quite similar to each other as expected, since stars in the target galaxy make up a large portion of the mass of the total disk.

Examining the values of v_c of the individual disk particles (top rows of (a)–(g) in Figure 10), stellar particles having relatively high values of v_c (out of the six bins as indicated by the color bar) appear dominantly in the inner region of the disk around the bar and the arms where the density of stars is high as well. Whereas, stars having lower values of v_c are spread more widely over the disk. It should be noted that many stars whose values of v_c falling in different bins overlap spatially. (E.g., stars lying in the innermost region of the disk have diverse values of v_c , ranging from all of the six bins.) On the other hand, gas particles having lower values of v_c are found in the inner region of the disk and those having different values of v_c hardly overlap spatially. This is because, unlike stars, dynamically cold gas responds very quickly to the potential perturbations arisen by the galactic structures such as bar and spiral arm (Roberts 1969; Oh et al. 2008). Hence shocks can easily occur on the gas disk causing the gas to lose angular momentum (Kim & Kim 2014; Kim et al. 2014). For instance, the shocks driven by the asymmetric bar-potential can generate torques through which gas loses the angular momentum and moves radially inward; the spiral shocks can also work to remove

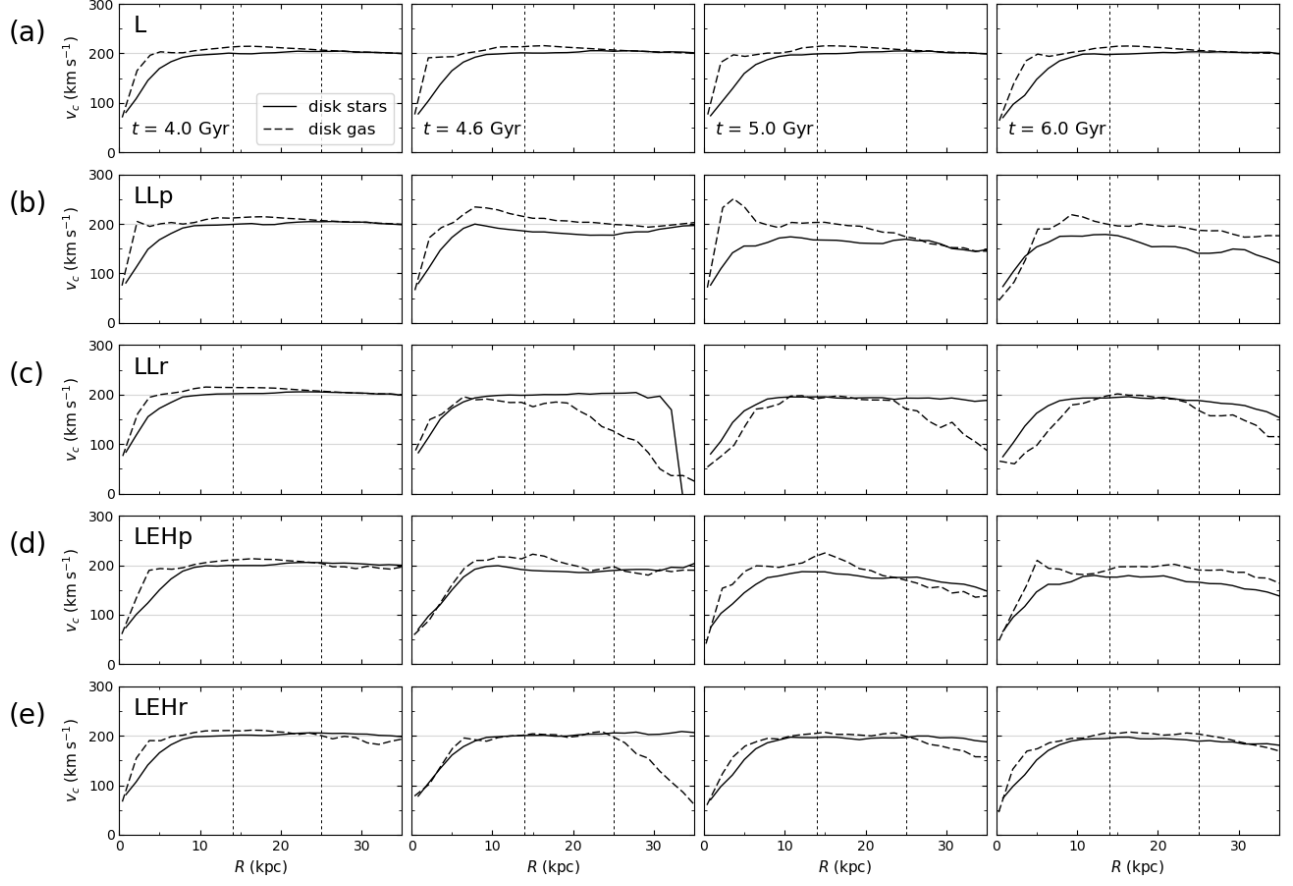


FIG. 7.— Mass weighted, cylindrically averaged circular velocity v_c of the disk particles of the target galaxy with respect to the cylindrical radius R from runs L (a), LLp (b), LLr (c), LEHp (d), and LEHr (e). The leftmost through rightmost columns show the circular velocity profiles at $t = 4, 4.6, 5,$ and 6 Gyr, respectively. In each panel, solid curve represents the profile of the disk star particles (i.e., both old and young disk stars, if there are any young stars formed by the time) and dashed curve displays that of the disk gas particles (i.e., both non-star-forming and star-forming gas). The two vertical dotted lines mark R_{14} and R_{25} . In (b) through (e), the velocity profiles are estimated including the captured particles (i.e., those originally set as the disk stars or gas particles of the companion but transferred to the target), if there are any.

the angular momentum of the gas facing with the “pile up” of material.

3.2.2. Run LLp

Figures 7(b) and 8 (middle row) show the profiles of v_c and v_R , respectively, of the disk particles of the target galaxy experiencing a prograde collision with a late-type companion. First, examining the profiles of the disk stars in the region within R_{25} ³ (half the closest approach distance), there is a clear tendency for stars to lose v_c but gain both v_{R+} and v_{R-} after the prograde collision. The decrease in circular motions for stars is mainly due to the deflection of the orbits by tidal disruption: (Although there are some particles transferring from the companion to the target, we have found that their contribution is not significant in shaping the overall velocity profiles.) As shown in Figure 10 (bottom two rows of (a)–(g)), when the stellar disk of the target galaxy is pulled out by the tidal force, producing a bridge on the near-side

(to the companion) and a counter-tail on the far-side, stars located in the outermost part of the disk are pulled first radially outward and then those in the next outermost part follow, while the disk rotates and moves. This may have caused the phase coherence of the stellar orbits along the arms, making the distribution of v_c as appeared in the figure. (Note that many stars with different values of v_c overlap spatially, as in run L.) Since the stellar disk is strongly disturbed by the prograde collision and generate a substantial bridge and tail lasting a couple of giga years, the tendency of losing circular motion and gaining both radially inward and outward motions for stars (compared with those of before or without the collision) is maintained until $t = 6$ Gyr.

Next, as for the disk gas particles of the target galaxy, the circular and radial velocity profiles appear to vary more complicatedly after the collision, compared with those of stars: First of all, the amplitude of the circular velocity profile of gas does not generally decrease after the collision, but it rather fluctuates, sometimes making some inner peak(s) - e. g., as at $t = 5$ Gyr near $R = 3$ kpc (which will be discussed below). In addition, the amplitudes of the profiles of both v_{R+} and v_{R-} increase at $t = 5$ Gyr, until not long after the collision, and then slow down at $t = 6$ Gyr. During the collision, as

³ We consider/compare the profile of v_c from each of our runs only in the region within R_{25} throughout this paper - i.e., up to half the closest approach distance in the galaxy-galaxy encounter runs. That is because the outer part of the disk, further than R_{25} , of the target galaxy in some of our runs (particularly in runs LLp and LEHp) is severely disturbed through the interaction.

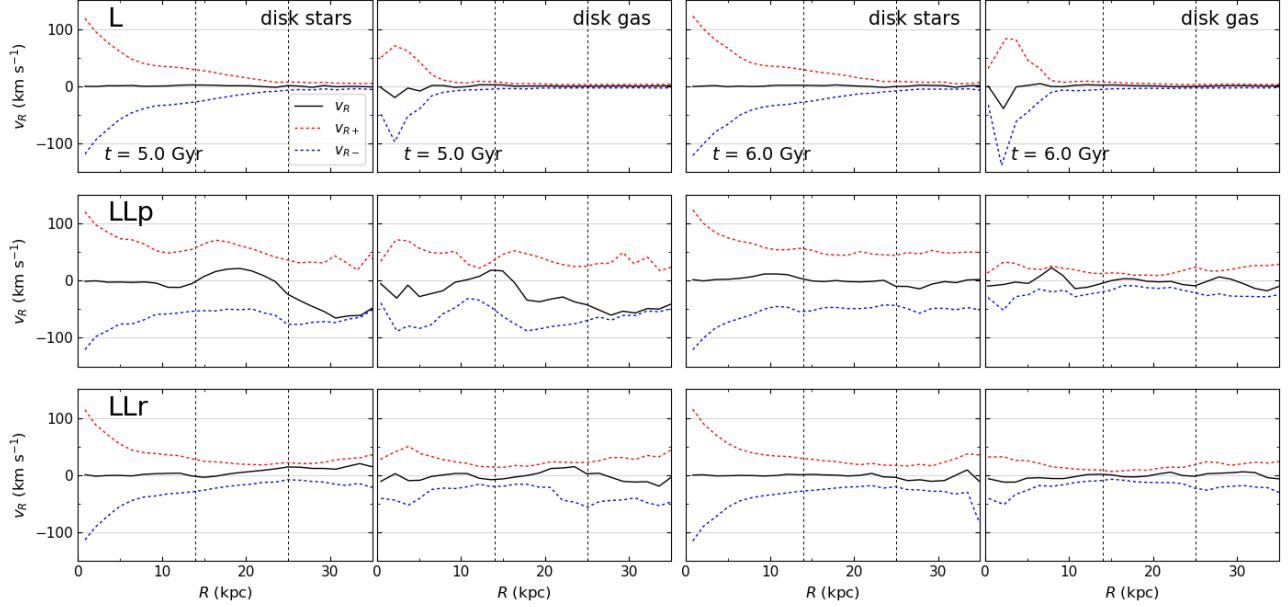


FIG. 8.— Mass weighted, cylindrically averaged radial velocity v_R of the disk particles of the target galaxy with respect to the cylindrical radius R from runs L (top row), LLp (middle row), and LLr (bottom row). The left two columns present the velocity profiles of the stars and gas, respectively, at $t = 5$ Gyr; similarly, the right two columns show those of the stars and gas at $t = 6$ Gyr. In each panel, the black solid curve represents the profile of v_R ; the red and blue dotted curves show those of v_{R+} and v_{R-} separately. The two vertical dotted lines indicate R_{14} and R_{25} . In the middle and bottom rows, the velocity profiles are estimated including the captured particles from the companion galaxy, if there are any.

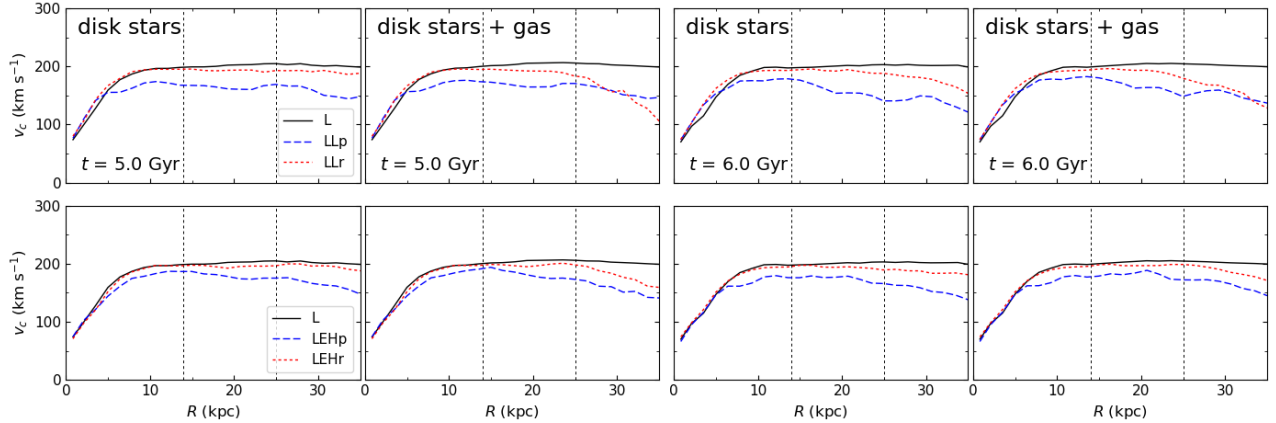


FIG. 9.— Top row: comparison of the circular velocity profiles of the disk material of the target galaxy from runs L, LLp, and LLr (black solid, blue dashed, and red dotted curves, respectively). The left two columns show the profiles of the disk star particles and of the all disk (stars + gas) particles, respectively, at $t = 5$ Gyr; similarly, the right two columns represent those of the stars and of the star + gas, respectively, at $t = 6$ Gyr. In each panel, the two vertical dotted lines mark R_{14} and R_{25} . Bottom row: same as the top row, but for runs L, LEHp, and LEHr.

shown in Figure 10 (see also Figure 6(a)), the gas disk of the target galaxy is pulled out by the gravitational tide, starting from the outskirts of the disk. Besides, the gas disk is also shock-compressed by the collision with the gas disk of the companion, starting from the leading side of the disk, while it rotates and moves. As stated previously, since dynamically cold gas responds very quickly to the density perturbations generated on the disk, gas particles having different values of v_c hardly overlap spatially, in contrast with the case of stars. Locally, some disk gas particles can gain the circular velocities through the collision, under the influence of the collisional compression and the shocks generated on the disk in addition to that of gravity. For example, the gas particles of the target galaxy at $t = 5$ Gyr lying along the asymmetric

inner arm around $R = 3$ kpc (those shown in pink in the middle row sixth panel from the left in Figure 10(a)) gain circular velocities, resulting in the peak around the radius in the profile of v_c . Interestingly, at $t = 5$ Gyr, the gas particles transferring to the target galaxy through the bridge (formed out of the gas disk of the companion) reaching the region near $R = 5$ kpc (measuring from the center of the target; those shown in green and red in the bottom row sixth panel from the left in Figure 10(a)) have particularly high circular velocities. It has occurred because the direction of progress of the gas bridge happens to be aligned with the direction of the local circular velocity in the target galaxy. In this particular case, however, the amount of the transferring gas is revealed to be not enough to make a significant contribution to

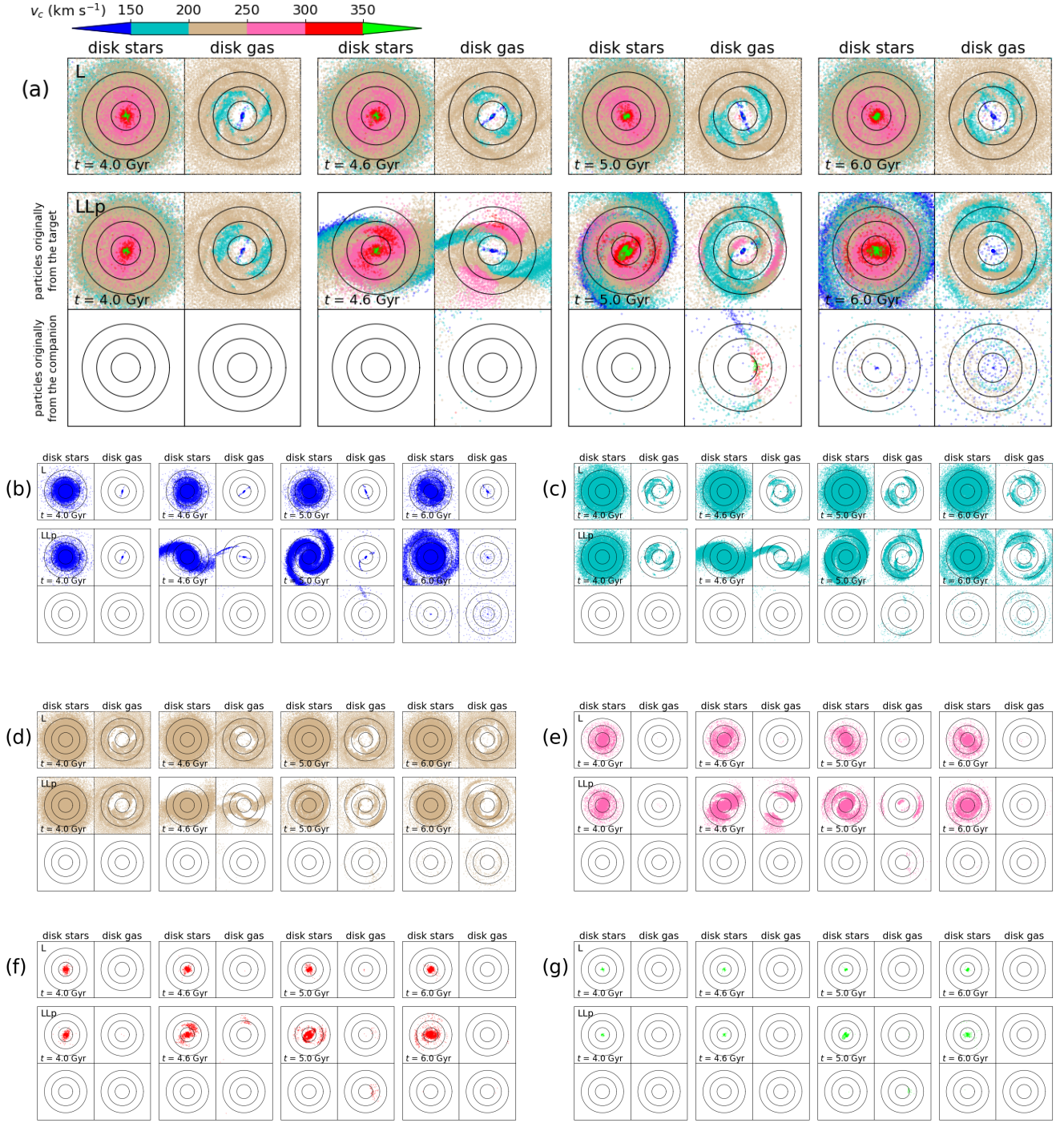


FIG. 10.— (a) Disk star and gas particles of the target galaxy from runs L and LLp at $t = 4, 4.6, 5$, and 6 Gyr (from leftmost two columns to rightmost two columns in order, respectively). The disk particles of the target galaxy from run L is shown in the top row; for run LLp, the disk particles originally set as the target galaxy and those initially set as the companion galaxy but transferred to the target galaxy are displayed separately in the middle and bottom rows, respectively. The particles are differently colored by the values of their circular velocities v_c as indicated in the color bar. (For simplicity, the particles having negative values of v_c are not distinguished, as they are not significant in runs L and LLp, for the purpose of this figure.) The particles having the lowest values of v_c are plotted first and then those having higher values of v_c are overlaid on top in order. Each panel measures 40 kpc on a side. The concentric solid circles in each panel measure $R = 5, 10$, and 15 kpc from the center of the target galaxy. (b)–(g) Same as (a) but displaying the particles separately depending on the values of their circular velocities: $0 \leq v_c < 150 \text{ km s}^{-1}$ (b), $150 \text{ km s}^{-1} \leq v_c < 200 \text{ km s}^{-1}$ (c), $200 \text{ km s}^{-1} \leq v_c < 250 \text{ km s}^{-1}$ (d), $250 \text{ km s}^{-1} \leq v_c < 300 \text{ km s}^{-1}$ (e), $300 \text{ km s}^{-1} \leq v_c < 350 \text{ km s}^{-1}$ (f), and $350 \text{ km s}^{-1} \leq v_c$ (g).

the profile of v_c .

We compare in Figure 9 (top row) the circular velocity profiles of the disk star particles and of the all disk

particles of the target galaxy at $t = 5$ and 6 Gyr (blue dashed curves). The profile of the all disk particles generally follows that of the stars only, as in run L. It is

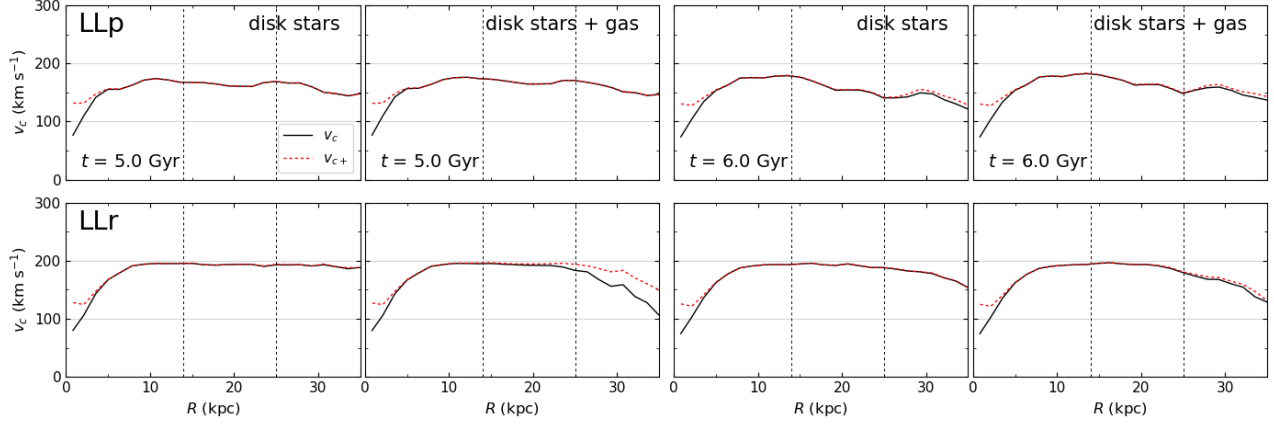


FIG. 11.— Comparison of the profiles of v_c and v_{c+} (black solid and red dotted curves, respectively) for the disk particles of the target galaxy from runs LLp (top row) and LLr (bottom row). The left two columns show the profiles of the disk star particles and of the all disk particles, respectively, at $t = 5$ Gyr; the right two columns shows those at $t = 6$ Gyr. In each panel, the two vertical dotted lines mark R_{14} and R_{25} .

because stars are dominant in mass on the disk and the encounter is not so strong as to make the system to be out of equilibrium. It is also clearly shown that both profiles of the stars and the star + gas from this run are well below those from run L after the collision, except in the central region. In addition, we examine how the circular velocity profile changes when excluding counter-rotating disk particles. Figure 11 displays that the profiles of v_{c+} of the stars and of the stars + gas (excluding counter-rotating ones) are quite similar to the profiles of v_c after the prograde collision, except at the central region. (Note that some difference between the profiles of v_c and v_{c+} also appears at the central region of the isolated target galaxy, as similarly as those in run LLr (bottom row)).

3.2.3. Run LLr

When the target galaxy experiences a retrograde collision with a late-type companion, the profile of v_c (Figure 7(c)) of the disk stars within R_{25} remains relatively unchanged after the collision. The amplitudes of both profiles of v_{R+} and v_{R-} of the stars (bottom row of Figure 8) also do not change much through the retrograde collision. As for the disk gas within R_{25} , the profiles of v_c , v_{R+} , and v_{R-} change somewhat after the collision (except during or shortly after the collision), but not as greatly as in run LLp. Figure 9 (top row) also shows that the circular velocity profiles of the stars and of the star + gas from this run do not differ much from those from run L at $t = 5$ and 6 Gyr. Figure 11 (bottom row) presents the profiles of v_c and v_{c+} of the disk particles. The two profiles within R_{25} are generally similar, except at the central region of the disk.

This result indicates that the retrograde collision considered here has not been able to drive significant dynamical response in the target galaxy, in contrast with the case of the prograde collision, despite of the equally close encounter. Therefore, it can be inferred that when a pair of galaxies are observed to be close to each other, the effects on the kinematics of a system by the interaction with its neighbour could be too weak to be measured, depending on the geometry of the encounter.

3.2.4. Runs LEHp and LEHr

Let's first consider run LEHp, where the target galaxy interacts with an early-type companion in prograde sense. As shown in Figures 7(d) and 9, the profile of v_c of the disk stars of the target galaxy evolves somewhat similarly to that from run LLp, after the collision - i. e., stars generally lose v_c after the collision. Since the gravitational pull exerted upon the target galaxy depends on the mass of the companion, and which is the same in runs LEHp and LLp, the stellar orbits in the target galaxy from both runs are influenced in a similar way through the prograde collision.

For the disk gas of the target galaxy from run LEHp, the profile of v_c becomes somewhat bumpy, without a marked decrease, after the collision. This trend has also been found in that of the gas from run LLp. However, the specific shape of the profile from this run evolves differently from that from run LLp after the collision. This may have been caused by the different hydrodynamic interactions in these runs.

Finally for run LEHr (Figures 7(e) and 9), where the target galaxy experiences a retrograde collision with an early-type companion, the profile of v_c of the disk stars of the target galaxy remains almost unchanged after the collision, similarly as that from run LLr. The velocity profile of the gas varies after the collision but only slightly. As pointed out in Section 3.2.3, it means that the dynamics of the target galaxy in this run, as well as in run LLr, is not affected significantly by the retrograde collision, except the outskirts of the disk.

3.2.5. Angular Momentum

We calculate the spin angular momentum S of the target galaxy disk from all of our runs. For the estimation of $S(R)$, we consider the disk particles of the target galaxy enclosed within a cylindrical region of a radius R (with $|z| \leq 20$ kpc). We present in Figure 12 the evolutions of $S(R_{25})$ and $S(R_{14})$. It is shown that S of the star disk and of the star + gas disk of the target galaxy decrease drastically after the prograde collision (runs LLp and LEHp), but not after the retrograde collision (runs LLr and LEHr). Specifically, the value of $S(R_{25})$ of the star + gas disk at $t = 5.5$ Gyr (i.e., 1 Gyr after the collision) is about 20 % (15 %) smaller in run LLp(LEHp) than that at $t = 3.5$ Gyr (1 Gyr before

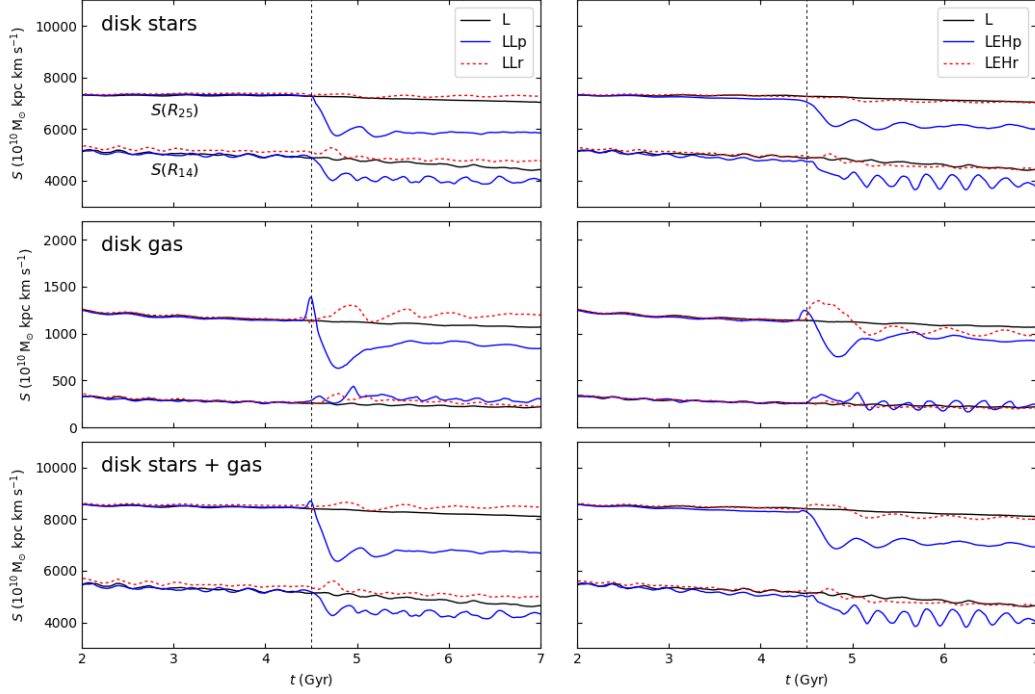


FIG. 12.— Spin angular momentum of the disk of the target galaxy with respect to time from runs L, LLp and LLr (left column) and runs L, LEHp, and LEHr (right column). The top through bottom rows show the angular momentum of the disk, considering the disk stars (top row), gas (middle row), and stars + gas (bottom row) particles enclosed in a cylindrical region of a radius R ($S(R)$, with $|z| \leq 20$ kpc). In each panel, the upper and lower three curves display $S(R_{25})$ and $S(R_{14})$, respectively. (The particles captured by the target from the companion are included, if there are any.) The vertical dotted line indicates the closest approach time, $t = 4.5$ Gyr, between the target and the companion galaxies in the galaxy-galaxy encounter runs.

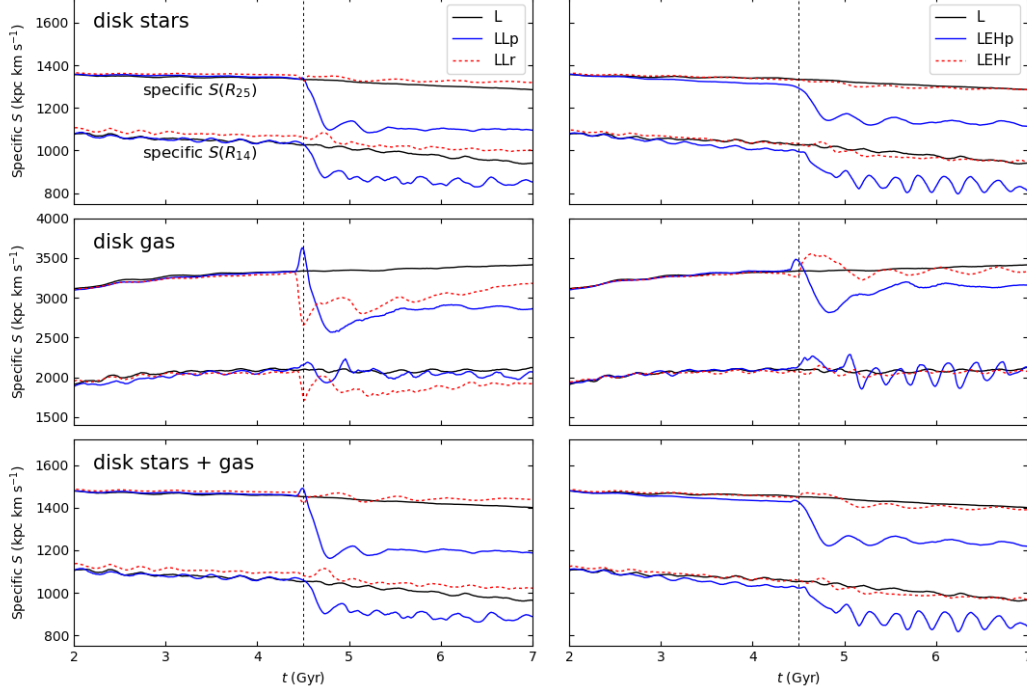


FIG. 13.— Same as Figure 12, but for the specific angular momentum of the disk of the target galaxy.

the collision). In Figure 13, we also present the specific angular momentum of the disk of the target galaxy, by dividing S by the total mass of the enclosed particles in each case. The specific angular momentum of the disk also decreases clearly after the prograde collision, simi-

larly to the angular momentum. This phenomenon can be interpreted as follows: Initially, in the center-of-mass (CM) frame, two galaxies are far apart and approach linearly each other. After the encounter, those galaxies rotate about the CM with the orbital angular momen-

tum L , and the total angular momentum of this system is given by the vector sum of \vec{S} and \vec{L} of those galaxies. The sum is additive in magnitude in the prograde case, but subtractive in the retrograde case. This results in the decrease of S of the target galaxy disk in the prograde case while the increase of that in the retrograde case. This justifies our result showing the different behavior of S in the prograde case against the retrograde case. The contribution of the tidal effects on the target galaxy disk discussed in the previous sections decreases S further, in such a way that the decrease of S in the prograde case is enhanced and the increase of S in the retrograde case is reduced. The change of L is biggest right after the encounter, and one can see such a drastic change of S as shown in Figure 12. There could be also the tidal effects due to the bulge and the DM halo reducing S of the galaxy disks in both of the prograde and retrograde cases, but those contributions are not significant. We will discuss such subdominant effects briefly in Appendix B.

4. SUMMARY AND DISCUSSION

Influenced by observational studies that found some correlations between the spin magnitudes in pairs of galaxies (Cervantes-Sodi et al. 2010; Lee et al. 2018a), we have carried out this numerical study in order to examine how the spin of LTGs is affected by interactions, in a more direct way. As the first in a series of (planned) work, we have constructed four simulations of co-planner encounters between a late-type target galaxy (model L) and an equally massive companion galaxy, whose morphology is either a late- or an early-type (model L or EH, respectively), in prograde or retrograde sense. They are the LLp, LLr, LEHp, and LEHr runs. We have also set up one simulation of the evolution of the target galaxy in isolation, run L, for comparison.

By analysing the circular velocities of the disk particles of the target galaxy (up to R_{25}) over time from each of our five runs, we have obtained the following results:

1. Disk stars of the late-type target galaxy tend to lose the circular velocities (and to gain both positive and negative radial velocities) through the prograde collision in runs LLp and LEHp, regardless of the type of the companion. It is mainly due to the deflection of the orbits caused by the tidal disruption. Since the masses of the late- and the early-type companions (having the identical DM halo component) are the same, the individual disk stars (which are mainly affected by gravitational force) of the target galaxy in these runs dynamically evolve in a similar way through the collision.

2. Disk gas of the target galaxy does not generally lose the circular velocity through the prograde collision in runs LLp and LEHp. The circular velocity of the gas varies in a more complicated fashion, than those of the stars, due to the combined effects of the gravitational and the hydrodynamic interactions.

3. In case of the retrograde collision (runs LLr and LEHr), the circular velocities of the disk stars of the target galaxy remain almost unchanged after the collision, as similarly as those in the isolated target galaxy (run L). The circular velocity of the gas changes after the retrograde collision, but not as greatly as in runs LLp and LEHp, except during/near the collision. It indicates

that the retrograde collision in these runs does not drive a significant dynamical response in the target galaxy, irrespective of the type of the companion.

Since stars in our target galaxy make up a large portion of the mass of the total disk, as does in many well observed LTGs, the circular velocity profile of the entire disk material (stars + gas) generally follows that of the stars in all of our runs. It is also because the encounters considered here are not so strong as to make the systems to be out of equilibrium. Taken together, our simulation results indicate that the overall spin of a LTG can decrease through a prograde collision, but hardly through a retrograde collision, regardless of the morphology of the companion. It was also demonstrated in the time change of the spin angular momentum of the disk of the target galaxy. We have found that the angular momentum clearly decreases after the prograde collision, but not after the retrograde collision. This is due to the combined contributions of the tidal effect on the target disk and the spin-orbits interactions (followed by the total angular momentum conservation) of the two galaxies. Specifically, the spin angular momentum (within R_{25}) decreased by $\sim 20\%$ and $\sim 15\%$ after the prograde collision in runs LLp and LEHp, respectively. We can thus infer that, for a sample of LTGs which are observed to have a close neighbour of a comparable mass, the tendency of decrease of the spin of the LTGs (as the separation distance decreases) would be more clearly measured when the sample includes many LTGs that experiences and/or have experienced one or more prograde collisions.

The results from this work may not be generalized to different cases. For example, in case where a late-type target galaxy interacts with a companion galaxy of a highly unequal mass, a significant net amount of material can transfer from one galaxy to the other. Let us recall that, in run LLp at $t = 5$ Gyr, there were some gas particles transferring from the companion to the target through the narrow bridge, having much higher circular velocities than surrounding particles. Their higher circular velocities could be made because the direction of progress of the bridge happened to be aligned with the direction of the local circular velocity. The amount of the transferring material in run LLp was not enough to make a meaningful impact in shaping the circular velocity profile of the entire disk material. However, in different situations such as interactions between unequal mass galaxies, a sufficient amount of material might be able to transfer to the target galaxy with high circular velocities, resulting in a peak in the circular velocity profile at the corresponding radius.

Another example, when a gas-rich late-type target galaxy interacts strongly with another gas-rich galaxy, hydrodynamic effects of the interaction may play a much more influential role than in our runs. In this case, the amplitude of the circular velocity profile of the overall disk material of the target galaxy might not simply decrease after the collision, unlike in our runs LLp and LEHp (where tidal disruption plays a bigger role to decrease the amplitude), but changes in a very complex fashion depending on the particular circumstance of each case.

We end this work by emphasizing the significance of interactions with neighbouring galaxies in determining the spin of LTGs at current stage, as demonstrated by

our runs LLp and LEHp. Since most galaxies experience multiple interactions over the course of their lifetime, the accumulated effects of galaxy-galaxy interactions at later stages after the acquisition of the internal angular momentum will play a crucial role in the evolution of the total angular momentum of galaxies. We will continue studying this subject in our future work, considering more diverse interactions including the cases stated above and also major and minor mergers for a more in-depth understanding of the evolution of galactic spin in various environments.

We thank the referee Santi Roca-Fàbrega and the anonymous referee very much for insightful comments and helpful suggestions which improved this paper significantly. J.-S. H. is grateful to Juhan Kim and Yonghui Kim for helpful discussions. We appreciate Joshua E. Barnes making the ZENO code available and Volker Springel for providing us with GADGET-3. We thank the Korea Institute for Advanced Study for providing computing resources (Higgs Server and KIAS Center for Advanced Computation Linux Cluster System) for this study. This work was supported by Basic Science Research Program through the National Research Foundation of Korea (NRF) funded by the Ministry of Education under the Grant Nos. NRF-2018R1D1A1B07048156 (J.-S. Hwang) and NRF-2018R1D1A1B07050701 (J.-S. Hwang), and NRF-2020R1I1A1A01072816 (S.-h. Nam), and also funded by the Ministry of Science and ICT under the Grant No. 2020R1A2C3009918 (S.-h. Nam).

APPENDIX A Run LLr2

We have performed one more simulation, “run LLr2”.

The only difference between the initial conditions of this run and run LLr is the direction of the initial spin of the companion galaxy - i. e., it is set with a counterclockwise direction in run LLr2. Therefore, when the target and the companion meet most closely, both galaxies experience the encounter with the other as retrograde.

We present the snapshots (Figures 14, and 15) and the circular velocity profiles (Figure 16) from run LLr2. Both target and the companion galaxies do not develop substantial bridges and tails after the retrograde encounter as expected. The overall circular velocity of the disk material of the target galaxy does not decrease much after the collision as shown in Figure 16. The total spin angular momentum becomes doubles in this case so that the change of the spin angular momentum is milder than that of run LLr (where the spin sum is subtractive due to the opposite spin directions) as one can see from the figure.

APPENDIX B Angular moment of various components

In Figure 17 we present the spin angular momentum $S(R_{25})$ of the various components of the target galaxy from run L, LLp, and LLr. The figure indicates that most of the spin angular momentum of the target galaxy’s disk is not transferred to different components of the target galaxy; it is likely to be transferred to the orbital angular momentum of the two interacting galaxies. In order to have full access to the mechanism of angular momentum transfer of interacting galaxies, more extensive analysis are need to be done.

REFERENCES

- Anderson, M. E., & Bregman, J. N. 2010, Do Hot Halos Around Galaxies Contain the Missing Baryons?, *ApJ*, 714, 320
- Barnes, J. E. 2011, ZENO: N-body and SPH Simulation Codes, Astrophysics Source Code Library, record ascl:1102.027
- Barnes, J. E., & Hibbard, J. E. 2009, Identikit 1: A Modeling Tool for Interacting Disk Galaxies, *AJ*, 137, 3071
- Barnes, J., & Hut, P. 1986, A Hierarchical $O(N \log N)$ Force-calculation Algorithm, *Nature*, 324, 446
- Brook, C. B., Stinson, G., Gibson, B. K., et al. 2012, Hierarchical Formation of Bulgeless Galaxies - II. Redistribution of Angular Momentum via Galactic Fountains, *MNRAS*, 419, 771
- Cappellari, M. 2016, Structure and Kinematics of Early-type Galaxies from Integral Field Spectroscopy, *ARA&A*, 54, 597
- Casuso, E., & Beckman, J. E. 2015, On the Origin of the Angular Momentum of Galaxies: Cosmological Tidal Torques Supplemented by the Coriolis Force, *MNRAS*, 449, 2910
- Cervantes-Sodi, B., Hernandez, X., & Park, C. 2010, Clues on the Origin of Galactic Angular Momentum from Looking at Galaxy Pairs, *MNRAS*, 402, 1807
- Cloet-Osselaer, A., De Rijcke, S., Vandenbroucke, B., et al. 2014, Numerical Simulations of Dwarf Galaxy Merger Trees, *MNRAS*, 442, 2909
- Codis, S., Pichon, C., & Pogosyan, D. 2015, Spin Alignments within the Cosmic Web: a Theory of Constrained Tidal Torques near Filaments, *MNRAS*, 452, 3369
- Davis, A. J., & Natarajan, P. 2009, Angular Momentum and Clustering Properties of Early Dark Matter Haloes, *MNRAS*, 393, 1498
- Emsellem, E., Cappellari, M., Krajnović, D., et al. 2011, The ATLAS^{3D} Project - III. A Census of the Stellar Angular Momentum within the Effective Radius of Early-type Galaxies: Unveiling the Distribution of Fast and Slow Rotators, *MNRAS*, 414, 888
- Gingold R. A., & Monaghan J. J. 1977, Smoothed Particle Hydrodynamics: Theory and Application to Non-spherical Stars, *MNRAS*, 181, 375
- Graham, M. T., Cappellari, M., Li, H., et al. 2018, SDSS-IV MaNGA: Stellar Angular Momentum of about 2300 Galaxies: Unveiling the Bimodality of Massive Galaxy Properties, *MNRAS*, 477, 4711
- Hernquist, L. 1990, An Analytical Model for Spherical Galaxies and Bulges, *ApJ*, 356, 359
- Hoyle, F. 1949, On the Cosmological Problem, *MNRAS*, 109, 365
- Hwang, J.-S., Park, C., & Choi, J.-H. 2013, The Initial Conditions and Evolution of Isolated Galaxy Models: Effects of the Hot Gas Halo, *JKAS*, 46, 1
- Hwang, J.-S., & Park, C. 2015, Effects of Hot Halo Gas on Star Formation and Mass Transfer During Distant Galaxy-Galaxy Encounters, *ApJ*, 805, 131
- Hwang, J.-S., Park, C., Banerjee, A., & Hwang, H. S. 2018, Evolution of Late-type Galaxies in a Cluster Environment: Effects of High-speed Multiple Encounters with Early-type Galaxies, *ApJ*, 856, 160
- Katz, N., Weinberg, D. H., & Hernquist, L. 1996, Cosmological Simulations with TreeSPH, *ApJS*, 105, 19
- Kennicutt, R. C. Jr. 1998, The Global Schmidt Law in Star-forming Galaxies, *ApJ*, 498, 541
- Kim, W.-T., Kim, Y., & Kim, J.-G. 2014, Nature of the Wiggle Instability of Galactic Spiral Shocks, *ApJ*, 789, 68
- Kim, Y., & Kim, W.-T. 2014, Gaseous Spiral Structure and Mass Drift in Spiral Galaxies, *MNRAS*, 440, 208
- Kubryk, M., Prantzos, N., & Athanassoula, E. 2015, Evolution of the Milky Way with radial motions of stars and gas. I. The solar neighbourhood and the thin and thick disks, *A&A*, 580, 126
- Lee, J. C., Hwang, H. S., & Chung, H. 2018a, A Study of Environmental Effects on Galaxy Spin using MaNGA Data, *MNRAS*, 477, 1567
- Lee, J., Kim, S., Jeong, H., et al. 2018b, Wobbling Galaxy Spin Axes in Dense Environments, *ApJ*, 864, 69
- McMillan, P. J. 2011, Mass models of the Milky Way, *MNRAS*, 414, 2446

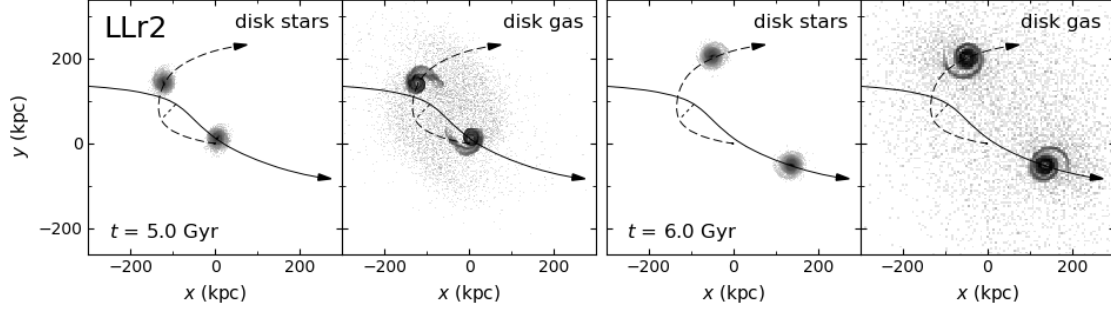


FIG. 14.— Same as Figure 5, but for run LLr2.

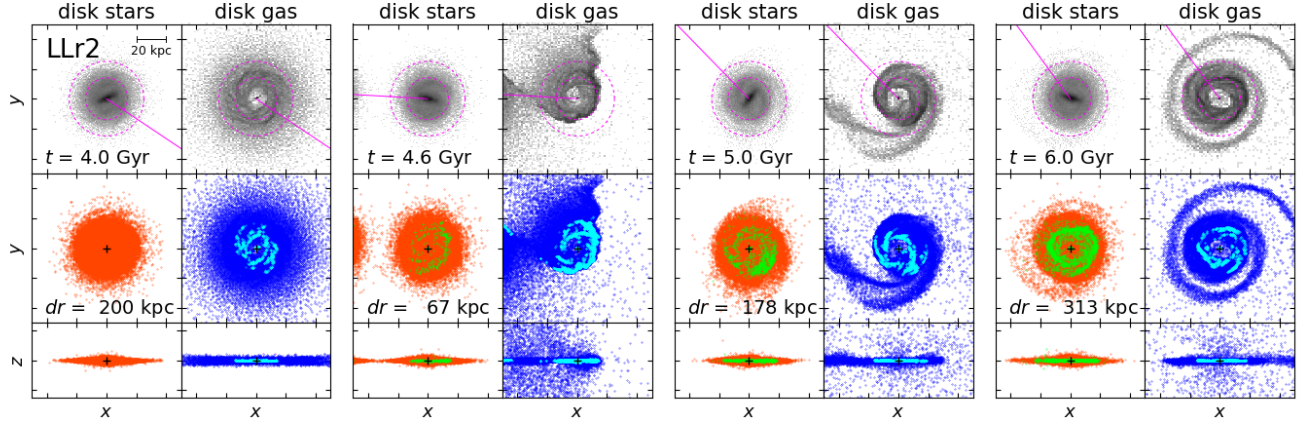


FIG. 15.— Same as Figure 3, but for run LLr2.

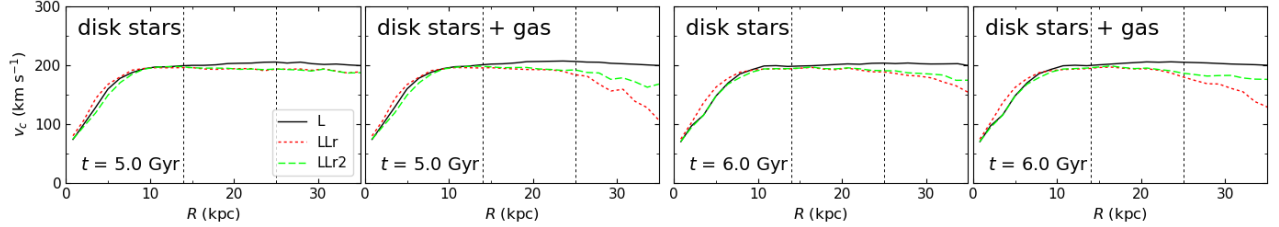


FIG. 16.— Same as Figure 9, but for runs L, LLr, and LLr2.

Navarro, J. F., Frenk, C. S., & White, S. D. M. 1996, The Structure of Cold Dark Matter Halos, *ApJ*, 462, 563
 Oh, S. H., Kim, W.-T., & Lee, H. M. 2008, Physical Properties of Tidal Features in Interacting Disk Galaxies, *ApJ*, 683, 94
 Peebles, P. J. E. 1969, Origin of the Angular Momentum of Galaxies, *ApJ*, 155, 393
 Porciani, C., Dekel, A., & Hoffman, Y. 2002, Testing Tidal-Torque Theory - I. Spin Amplitude and Direction, *MNRAS*, 332, 325
 Roberts, W. W. 1969, Large-Scale Shock Formation in Spiral Galaxies and its Implications on Star Formation *ApJ*, 158, 123
 Rodriguez-Gomez, V., Sales, L. V., Genel, S., et al. 2017, The Role of Mergers and Halo Spin in Shaping Galaxy Morphology, *MNRAS*, 467, 3083

Springel, V. 2005, The Cosmological Simulation Code GADGET-2, *MNRAS*, 364, 1105
 Springel, V., & Hernquist, L. 2002, Cosmological Smoothed Particle Hydrodynamics Simulations: The Entropy Equation, *MNRAS*, 333, 649
 Springel, V., & Hernquist, L. 2003, Cosmological Smoothed Particle Hydrodynamics Simulations: A Hybrid Multiphase Model for Star Formation, *MNRAS*, 339, 289
 Tempel, E., Stoica, R. S., & Saar, E. 2013, Evidence for Spin Alignment of Spiral and Elliptical/S0 Galaxies in Filaments, *MNRAS*, 428, 1827
 von Neumann, J. 1951, in Monte Carlo Method. National Bureau of Standards Applied Mathematics Series 12 (Washington, DC: US Government Printing Office), 36
 White, S. D. M. 1990, Angular Momentum growth in Protogalaxies, *ApJ*, 286, 38

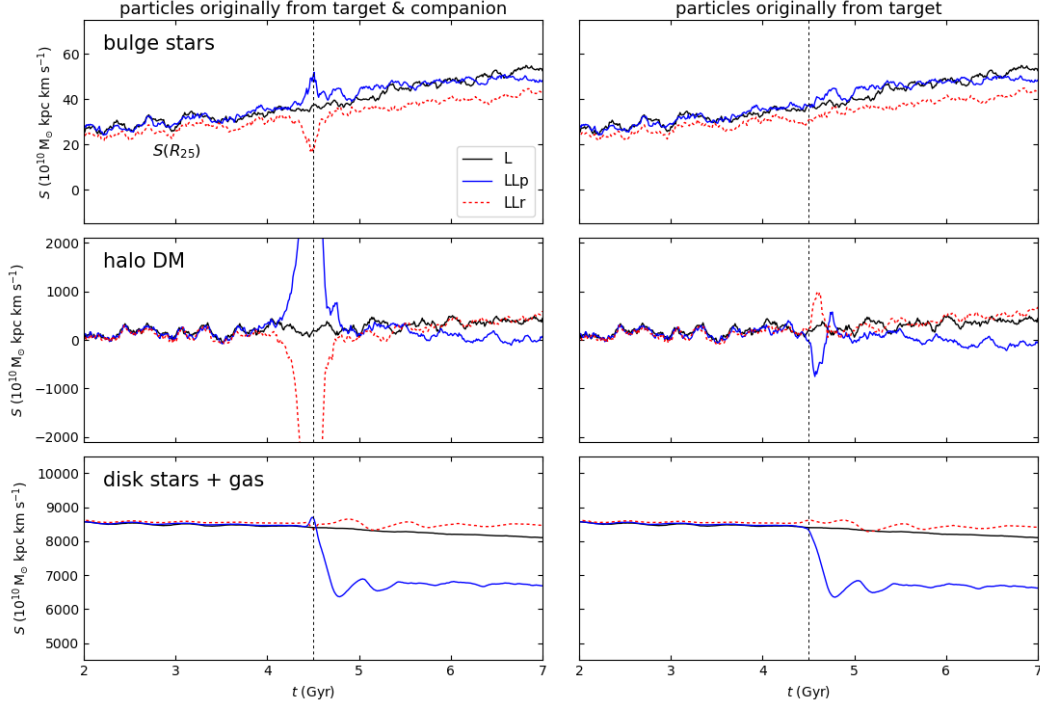


FIG. 17.— Spin angular momentum $S(R_{25})$ of the stellar bulge (top row), the DM halo (middle row), and the disk (bottom row) of the target galaxy with respect to time from runs L, LLp and LLr. In the calculation of $S(R_{25})$, only the mass within R_{25} and $|z| \leq 20$ kpc from the center of the target is considered. The left and right columns show the change of $S(R_{25})$, when all particles are used or when only the particles originally belonging to the target galaxy are used, respectively. In each panel the vertical dotted line indicates the closed approach time, $t = 4.5$ Gyr, between the target and the companion galaxies in the encounter runs.